Magnifying Superlens in the Visible Frequency Range

Igor I. Smolyaninov,* Yu-Ju Hung, Christopher C. Davis

We demonstrate a magnifying superlens that can be integrated into a conventional far-field optical microscope. Our design is based on a multilayer photonic metamaterial consisting of alternating layers of positive and negative refractive index, as originally proposed by Narimanov and Engheta. We achieved a resolution on the order of 70 nanometers. The use of such a magnifying superlens should find numerous applications in imaging.

Optical microscopy is an invaluable tool for studies of materials and biological entities. Imaging tools with ever-increasing spatial resolution are required if the current rate of progress in nanotechnology and microbiology is to continue. However, the spatial resolution of conventional microscopy is limited by the diffraction of light waves to a value on the order of 200 nm. Thus, viruses, proteins, DNA molecules, and many other samples are impossible to visualize with a regular microscope. One suggested way to overcome this limitation is based on the concept of a superlens (*1*), which relies on the use of materials or metamaterials that have negative refractive index in the visible frequency range. Near-field superlens imaging was recently demonstrated (*2*, *3*), but the technique is limited by the fact that the magnification of the planar superlens is equal to 1. Thus, a thin planar superlens cannot be integrated into a conventional optical microscope to image objects smaller than the diffraction limit.

We describe the realization of a magnifying superlens (Fig. 1A) and demonstrate its integration into a regular far-field optical microscope. Our design is based on the theoretical proposals of an "optical hyperlens" (*4*) and "metamaterial crystal lens" (*5*) and on the recently developed plasmon-assisted microscopy technique (*6*), and in particular on the unusual optics of surface plasmon polaritons (SPPs). The properties of these two-dimensional optical modes and convenient ways to excite them are described in detail in (*7*). The wave vector of the SPPs is defined by the expression

$$k_p = \frac{\omega}{c}\left(\frac{\varepsilon_d \varepsilon_m}{\varepsilon_d + \varepsilon_m}\right)^{1/2} \quad (1)$$

where $\varepsilon_m(\omega)$ and $\varepsilon_d(\omega)$ are the frequency-dependent dielectric constants of the metal and the dielectric, respectively, and c is the speed of light. Above the resonant frequency ω described by the condition

$$\varepsilon_m(\omega) \approx -\varepsilon_d(\omega) \quad (2)$$

the SPP group and phase velocities may have opposite signs (Fig. 1B). The internal structure of the magnifying superlens (Fig. 2A) consists of concentric rings of poly(methyl methacrylate) (PMMA) deposited on a gold film surface. For the SPP dispersion law for the gold-vacuum and gold-PMMA interfaces (Fig. 1B) in the frequency range marked by the box, PMMA has negative refractive index $n_2 < 0$ as perceived by plasmons (the group velocity is opposite to the phase velocity). The width of the PMMA rings d_2 is chosen so that $n_1 d_1 = -n_2 d_2$, where d_1 is the width of the gold-vacuum portions of the interface. Although the imaging action of our lens is based on the original planar superlens idea, its magnification depends on the fact that all the rays in the superlens tend to propagate in the radial direction when $n_1 d_1 = -n_2 d_2$ (Fig. 1A). This behavior was observed in the experiment upon illumination of the lens with $\lambda = 495$ nm laser light (bottom portion of Fig. 2B) for which $n_1 d_1 = -n_2 d_2$. The narrow beam visible in the image is produced by repeating self-imaging of the focal point by the alternating layers of materials with positive and negative refractive index. On the other hand, if 515-nm light is used, the lens becomes uncompensated and the optical field distribution inside the lens reproduces the field distribution in the normal "plasmonic lens" as described in (*8*) (top portion of Fig. 2B). However, in the complete theoretical description of the magnifying superlens, the ray optics picture presented in Fig. 1A may need to be supplemented by the anisotropic effective medium theory presented in (*4*, *5*).

The magnifying action of the superlens is demonstrated in Figs. 3 and 4. Rows of two or three PMMA dots were produced near the inner ring of the superlens (Fig. 3, B and C). These rows of PMMA dots had 0.5-μm periodicity in the radial direction, so that phase matching between the incident laser light and surface plasmons could be achieved (Fig. 1A). Upon illumination with an external laser, the three rows of PMMA dots in Fig. 3B gave rise to three radial divergent plasmon "rays," which are clearly visible in the plasmon image in Fig. 3D obtained with a conventional optical microscope. The cross-sectional analysis of this image across the plasmon "rays" (Fig. 3F) indicates resolution of at least 70 nm, or ~$\lambda/7$. The lateral separation between these rays increased by a factor of 10 as the rays reached the outer rim of the superlens. This increase allowed visualization of the triplet by conventional microscopy. In

Department of Electrical and Computer Engineering, University of Maryland, College Park, MD 20742, USA.

*To whom correspondence should be addressed. E-mail: smoly@eng.umd.edu

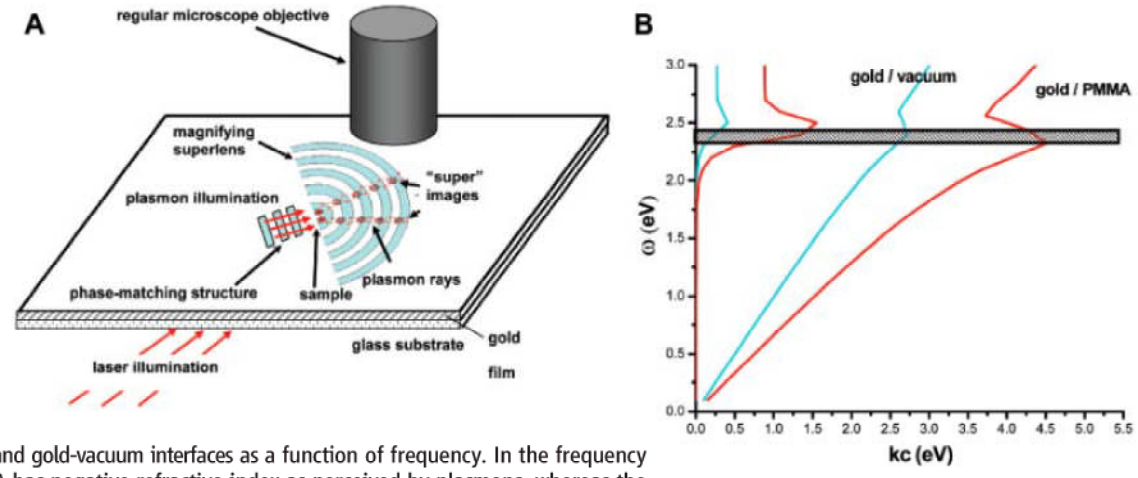

Fig. 1. (**A**) Schematic of the magnifying superlens integrated into a conventional microscope. The plasmons generated by the phase-matching structure illuminate the sample positioned near the center of the superlens. The lateral distance between the images produced by the alternating layers of materials with positive and negative refractive index grows with distance along the radius. The magnified images are viewed by a regular microscope. (**B**) Real and imaginary parts of the surface plasmon wave vector k at the gold-PMMA and gold-vacuum interfaces as a function of frequency. In the frequency range marked by the box, PMMA has negative refractive index as perceived by plasmons, whereas the gold-vacuum interface looks like a medium with positive refractive index.

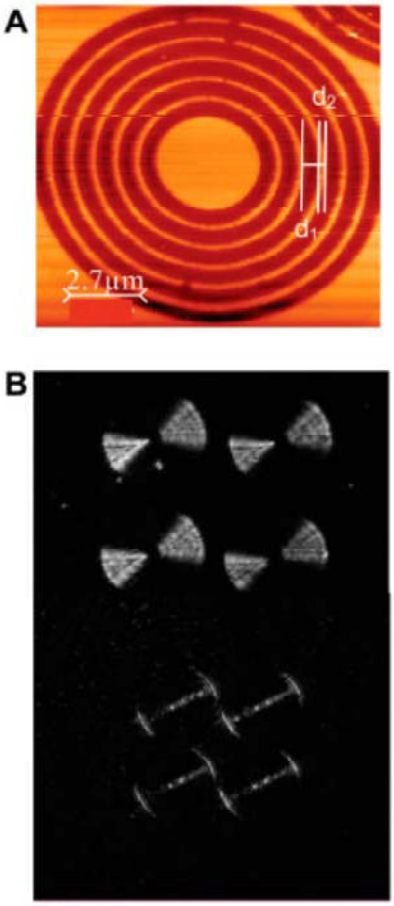

Fig. 2. (**A**) AFM image of the magnifying superlens made of PMMA rings on the gold film surface. (**B**) Optical field distribution in the magnifying superlens illuminated by external laser in the frequency ranges where $n_1d_1 \neq -n_2d_2$ (top) and $n_1d_1 = -n_2d_2$ (bottom).

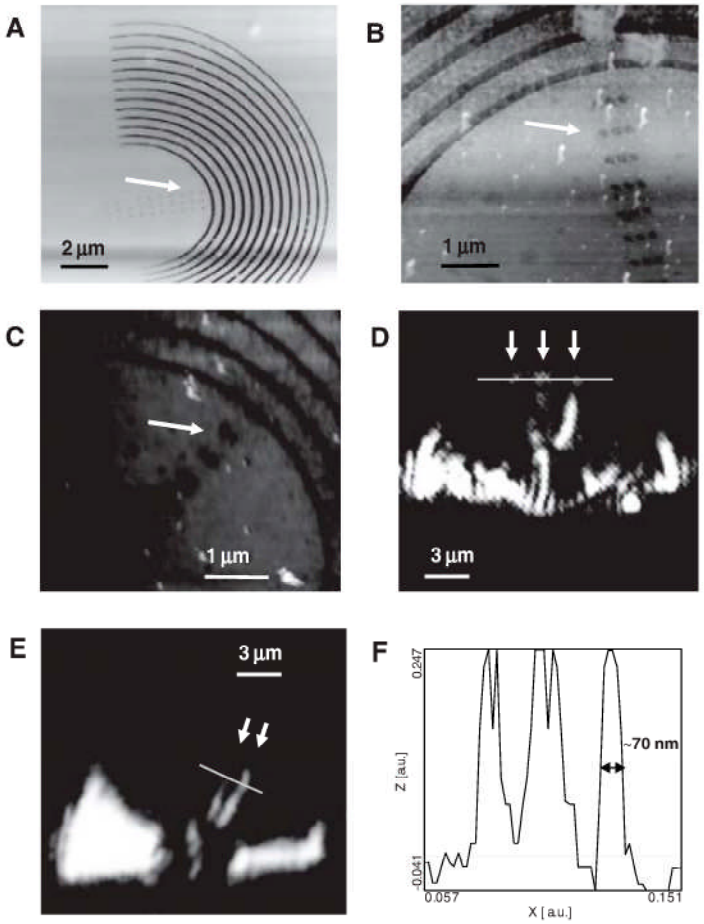

Fig. 3. AFM images (**A** to **C**) and conventional optical microscopy images (**D** and **E**) of the resolution test samples composed of three (A and B) and two (C) radial rows of PMMA dots (marked by arrows) positioned near the center of the magnifying superlens. The conventional microscopy images presented in (D) and (E) correspond to the samples shown in (B) and (C), respectively. The rows of PMMA dots give rise to either three or two divergent plasmon "rays" (marked by arrows), which are visible in the conventional optical microscopy images. (**F**) The cross section of the optical image along the line shown in (D) indicates resolution of at least 70 nm or ~ λ/7. Z, optical signal; X, distance.

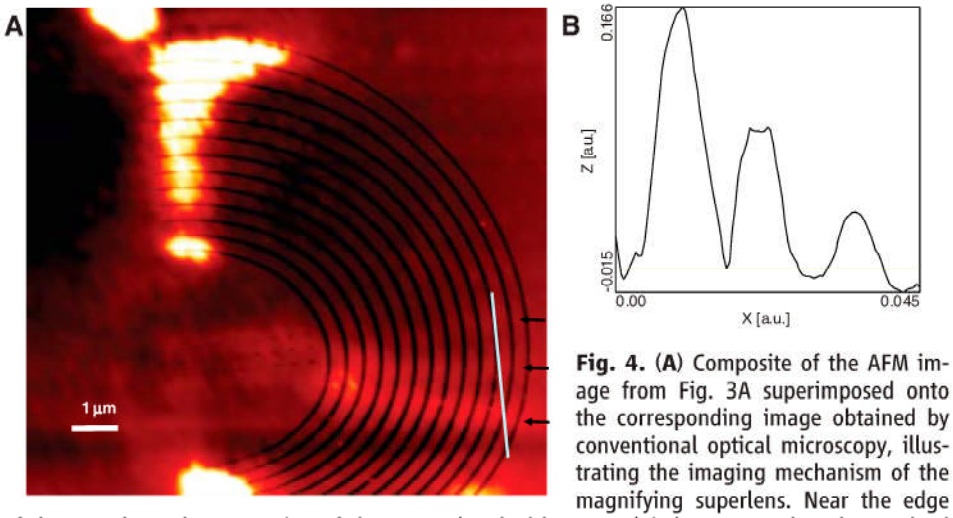

Fig. 4. (**A**) Composite of the AFM image from Fig. 3A superimposed onto the corresponding image obtained by conventional optical microscopy, illustrating the imaging mechanism of the magnifying superlens. Near the edge of the superlens, the separation of three rays (marked by arrows) is large enough to be resolved using a conventional optical microscope. (**B**) The cross section of the optical image along the line shown in (A) indicates the three rays.

a similar fashion, the two radial rows of PMMA dots shown in Fig. 3C gave rise to two plasmon rays, which are visualized in Fig. 3E.

The composite image in Fig. 4 is a superposition of the atomic force microscopy (AFM) image from Fig. 3A and the corresponding optical image obtained by conventional optical microscopy. It illustrates the imaging mechanism of the magnifying superlens: The passage of plasmon rays through the concentric alternating layers of materials with positive and negative refractive index increases the lateral separation of the three rays (marked by arrows at lower right). Near the edge of the superlens, the separation is large enough to be resolved with a conventional optical microscope, thus demonstrating a magnifying superlens in the visible frequency range.

The theoretical resolution of such a microscope may reach the nanometer scale (*1*, *4*). It thus has the potential to become an invaluable tool in medical and biological imaging, where far-field optical imaging of individual viruses and DNA molecules may become a reality. It allows very simple, fast, robust, and straightforward image acquisition.

We expect that unusual optical metamaterials may be designed and implemented using the principle of our magnifying superlens. Because $(d_1 + d_2)$ and the d_1/d_2 ratio (Fig. 2A) are easy to vary locally, the effective anisotropic refractive index of the multilayer material may be varied continuously from large negative to large positive values. Thus, unusual nanophotonic devices may be created in the visible frequency range, such as the recently suggested (*9*, *10*) and demonstrated (*11*) "invisibility cloak."

References and Notes

1. J. B. Pendry, *Phys. Rev. Lett.* **85**, 3966 (2000).
2. N. Fang, H. Lee, C. Sun, X. Zhang, *Science* **308**, 534 (2005).
3. D. O. S. Melville, R. J. Blaikie, *Opt. Express* **13**, 2127 (2005).

4. Z. Jacob, L. V. Alekseyev, E. Narimanov, *Opt. Express* **14**, 8247 (2006).
5. A. Salandrino, N. Engheta, *Phys. Rev. B* **74**, 075103 (2006).
6. I. I. Smolyaninov, C. C. Davis, J. Elliott, A. V. Zayats, *Phys. Rev. Lett.* **94**, 057401 (2005).
7. A. V. Zayats, I. I. Smolyaninov, A. A. Maradudin, *Phys. Rep.* **408**, 131 (2005).
8. Z. Liu, J. M. Steele, H. Lee, X. Zhang, *Appl. Phys. Lett.* **88**, 171108 (2006).
9. J. B. Pendry, D. Schurig, D. R. Smith, *Science* **312**, 1780 (2006); published online 24 May 2006 (10.1126/science.1125907).
10. U. Leonhardt, *Science* **312**, 1777 (2006); published online 24 May 2006 (10.1126/science.1126493).
11. D. Schurig *et al.*, *Science* **314**, 977 (2006); published online 18 October 2006 (10.1126/science.1133628).
12. Supported by NSF grants ECS-0304046 and CCF-0508213.

12 December 2006; accepted 8 February 2007
10.1126/science.1138746

Coupled Thermal and Hydrological Evolution of Tropical Africa over the Last Deglaciation

Johan W. H. Weijers,[1]* Enno Schefuß,[2]† Stefan Schouten,[1] Jaap S. Sinninghe Damsté[1]

We analyzed the distribution of branched tetraether membrane lipids derived from soil bacteria in a marine sediment record that was recovered close to the Congo River outflow, and the results enabled us to reconstruct large-scale continental temperature changes in tropical Africa that span the past 25,000 years. Tropical African temperatures gradually increased from ~21° to 25°C over the last deglaciation, which is a larger warming than estimated for the tropical Atlantic Ocean. A direct comparison with sea-surface temperature estimates from the same core revealed that the land-sea temperature difference was, through the thermal pressure gradient, an important control on central African precipitation patterns.

Continental climate change during the last deglaciation, especially in the tropics, is not as well understood as it is for the oceans (*1*–*3*). For Africa, a consensus is emerging on past changes in humidity and their causes based on lake level and pollen studies as well as the deuterium content of plant waxes (*4*–*6*), but temperature records for such tropical continental areas remain scarce and incomplete. In contrast to the marine environment, few quantitative temperature proxies exist for the terrestrial environment, and continuous long-term climate archives on land are limited. For instance, pollen-based vegetation studies, a widely used method for environmental reconstructions on land (*5*), are complicated in the tropics because the effects of changes in temperature are difficult to distinguish from those of changes in precipitation. Temperature estimates based on another method, stable oxygen isotope contents of carbonates and silicates, are widely applied in lacustrine sediments and speleothems. However, although these estimates are appropriate for high-resolution qualitative paleoclimate reconstructions (*7*, *8*), quantification of climate change in terms of paleotemperatures requires tenuous assumptions about the past changes in parameters that have influenced the source-water composition. The scant paleotemperature data available for the African continent imply a temperature difference of ~3.5° to 6°C between the Last Glacial Maximum (LGM) and the present day (*2*, *5*, *9*, *10*), but these data often represent a relatively local signal or are incomplete records. Thus, knowledge on African tropical temperature change over the last deglaciation is rather limited, especially for the vast tropical rainforest area of the Congo Basin. Continuous, high resolution, long-term records of continental-scale temperature change are much needed to improve this knowledge and enable proper comparison with records of marine temperature changes.

To gain better insight into the central African temperature development over the last deglaciation, its relation to global climatic changes, and its effect on the continental hydrological cycle, we used the Methylation index of Branched Tetraethers (MBT) and Cyclization ratio of Branched Tetraethers (CBT) based on branched glycerol dialkyl glycerol tetraethers (GDGTs) (*11*) present in a marine core recovered close to the Congo River outflow (GeoB 6518-1, 05°35.3′S, 11°13.3′E, water depth of 962 m, Fig. 1). Using the MBT and the CBT, we reconstructed the annual mean air temperature (MAT) of the Congo River basin (*12*) which could be compared with the sea surface temperature (SST) record obtained from the same core (Fig. 2). Branched GDGTs (fig. S1) are abundant core membrane lipids derived from bacteria that thrive in soils (*11*, *13*, *14*). As the soil erodes, the GDGTs are fluvially transported to the ocean. Indeed, they have been shown to be an excellent tracer of the fate of soil organic matter in the Congo deep-sea fan (*13*) and the Bay of Biscay (*15*) (fig. S2). The large catchment area of the Congo River (3.7×10^6 km^2) extends from about 6°N to 13°S and from about 13° to 33°E in central Africa (Fig. 1A), with elevations between 300 and 1200 m except for one small part, located at its eastern boundary, that rises above 2000 m (*16*). The temperature estimates obtained from our marine core, therefore, represent a catchment-integrated terrestrial temperature signal derived from land of low to intermediate elevation. Analysis of the

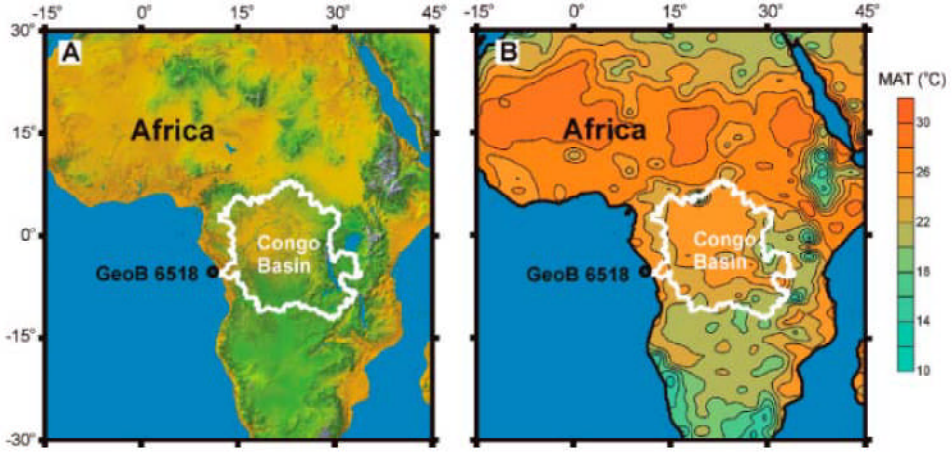

Fig. 1. Overview maps of Africa. The position of core GeoB 6518, recovered close to the Congo River outflow from a water depth of 962 m, and the extent of the Congo River drainage basin (white outline) are plotted (**A**) on a digital elevation map of Africa [picture from NASA Jet Propulsion Laboratory, California Institute of Technology] and (**B**) on a map showing the annual MAT distribution in Africa [available in the database in (*30*)].

[1]Royal Netherlands Institute for Sea Research, Department of Marine Biogeochemistry and Toxicology, Post Office Box 59, 1790 AB Den Burg–Texel, Netherlands. [2]Deutsche Forschungsgemeinschaft (DFG)–Research Center Ocean Margins, University of Bremen, Leobener Strasse, 28359 Bremen, Germany.

*To whom correspondence should be addressed. E-mail: jweijers@nioz.nl

†Present address: Institute for Geosciences, Christian-Albrechts-University Kiel, Ludewig-Meyn-Strasse 10, 28114 Kiel, Germany.